

**Supplementary information**

---

**Kinetic and energetic insights into the  
dissipative non-equilibrium operation of an  
autonomous light-powered  
supramolecular pump**

---

In the format provided by the  
authors and unedited

# Kinetic and energetic insights into the dissipative non-equilibrium operation of an autonomous light-powered supramolecular pump

Stefano Corra,<sup>‡,1,2</sup> Marina Tranfić Bakić,<sup>‡,1,2</sup> Jessica Groppi,<sup>1</sup> Massimo Baroncini,<sup>1,4</sup> Serena Silvi,<sup>1,3</sup> Emanuele Penocchio<sup>5</sup>, Massimiliano Esposito<sup>5</sup>, Alberto Credi<sup>1,2,\*</sup>

<sup>1</sup> CLAN-Center for Light Activated Nanostructures, Istituto ISOF-CNR, via Gobetti 101, 40129 Bologna, Italy

<sup>2</sup> Dipartimento di Chimica Industriale “Toso Montanari”, Università di Bologna, viale del Risorgimento 4, 40136 Bologna, Italy

<sup>3</sup> Dipartimento di Chimica “G. Ciamician”, Università di Bologna, via Selmi 2, 4126 Bologna, Italy

<sup>4</sup> Dipartimento di Scienze e Tecnologie Agro-alimentari, Università di Bologna, viale Fanin 44, 40127 Bologna, Italy

<sup>5</sup> Department of Physics and Materials Science, University of Luxembourg, L-1511 Luxembourg City, G. D. Luxembourg

<sup>‡</sup> these authors contributed equally to the work

## SUPPLEMENTARY INFORMATION

1. Materials and methods .....	2
2. Synthesis and characterization of the supramolecular pump .....	3
3. Operation of the Supramolecular Pump .....	6
4. Fitting and Numerical Simulations .....	10
5. Thermodynamic Analysis .....	14
7. References .....	23

## 1. Materials and methods

**General materials.** All reagents and chemicals were purchased from Sigma-Aldrich or VWR international and used as received unless otherwise stated. Flash column chromatography was performed using Sigma Aldrich Silica 40 (230-400 mesh size or 40-63  $\mu\text{m}$ ) as the stationary phase. Thin layer chromatography was performed on TLC Silica gel 60 F254 coated aluminum plates from Merck.

**NMR Spectroscopy.** NMR spectra were recorded on an Agilent DD2 spectrometer operating at 500 MHz. Chemical shifts are quoted in parts per million (ppm) relative to tetramethylsilane using the residual solvent peak as a reference standard and all coupling constants ( $J$ ) are expressed in Hertz (Hz).

**NMR Photochemistry** Photochemical reactions were performed in air-equilibrated  $\text{CD}_3\text{CN}$  solutions at 298 K inside NMR tubes in the spectrometer probehead, using a Prizmatix UHP-T-365-SR LED Illuminator (1.5 W,  $\lambda_{\text{max}} = 369$  nm, FWHM, 15.56 nm) equipped with an FCA-SMA adaptor for optical fiber. The desired irradiation wavelength of 365 nm was selected using the appropriate hard coated OD 4.0 bandpass filter. Neutral density AR coated filters were used to regulate intensity of incident light when required. Quartz optical fiber (core 1000  $\mu\text{m}$ , 5 m) equipped with a SMA connector on one end was purchased from Thorlabs. The other end of the optical fiber was scraped to remove the protective coatings, exposing the quartz core, and submerged into the solution within the NMR tube to be irradiated. The emission spectra of the light source (optical fiber end with protective coatings removed) were measured with an AVANTES Star Line AvaSpec-ULS2048CL-EVO-RS spectrometer. The emission intensity was selected using the appropriate neutral density filter with known optical density, purchased from Edmund Optics.

**Least square fitting and numerical simulations.** Fitting of the experimental data to the appropriate kinetic model was performed using Berkeley Madonna 10. Numerical simulations were performed with MATLAB R2018b implementing the kinetic model including all the kinetic and photokinetic equations as a system of differential equations that was solved numerically with ode15s solver.

## 2. Synthesis and characterization of the supramolecular pump

### 2.1 Synthesis of the axle

The axle was synthesized according to a previously published procedure.<sup>1</sup> Analytical data were in line with those previously reported.

### 2.2. <sup>1</sup>H NMR characterization of axles and complexes

<sup>1</sup>H NMR spectra of *E* and *Z* axles and complexes were consistent with those previously reported in ref. 1 and summarized in Fig. S1.

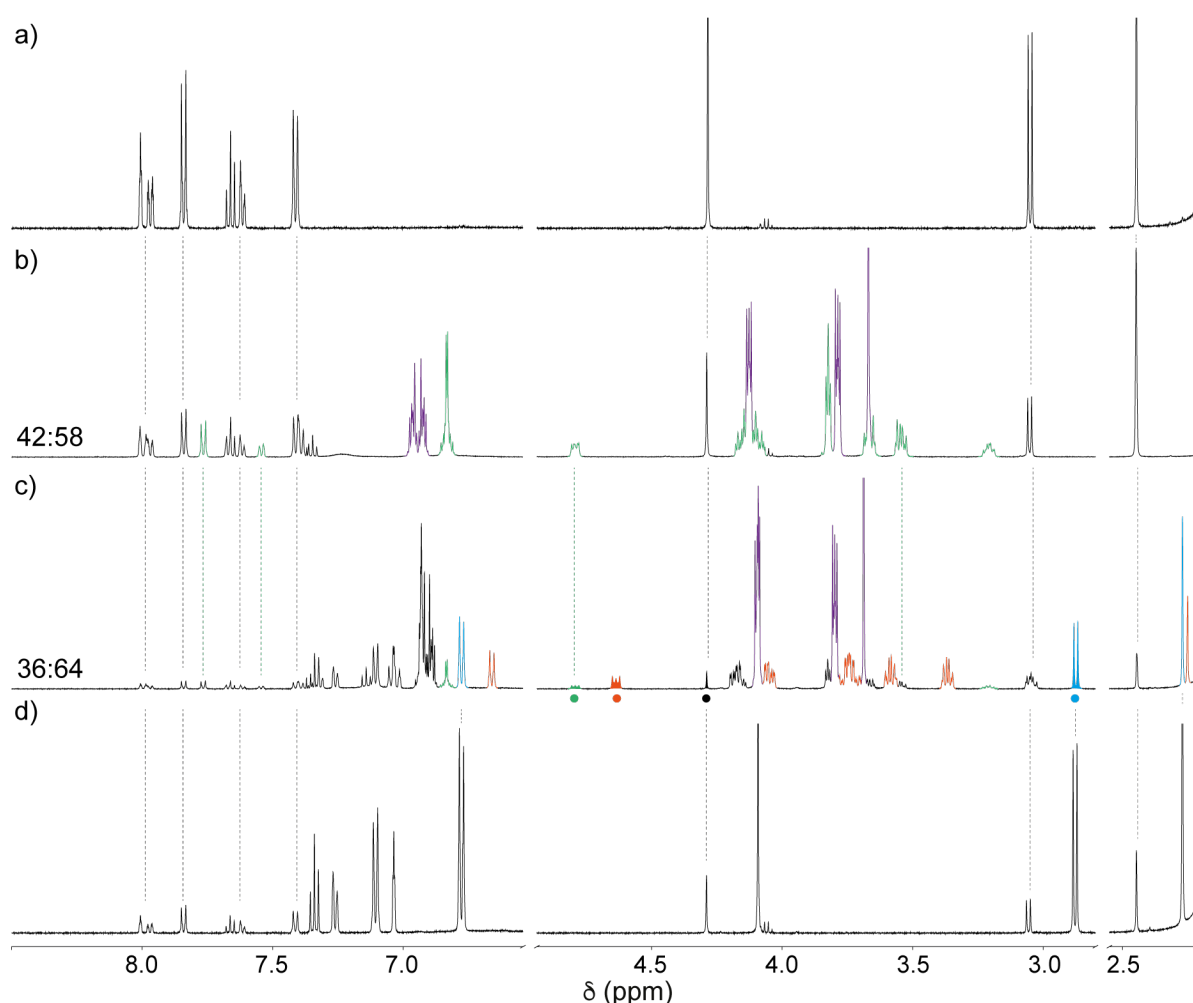


**Figure S1.** Typical <sup>1</sup>H NMR spectra (500 MHz, CD<sub>3</sub>CN, 298 K) of a) *E*-2<sup>+</sup>. b) A 1:1 equilibrated mixture of *E*-2<sup>+</sup> and **1**, the signals univocally associated with the complex are highlighted in green, the signals of free **1** are highlighted in purple. c) The same sample after exhaustive irradiation ( $\lambda_{irr} = 365$  nm, 30 min) and equilibration for 3 hours in dark. Signals of free *Z*-1<sup>+</sup> are highlighted in cyan, signals univocally attributed to the *Z*-complex are highlighted in orange. d) same sample as (a) after exhaustive irradiation ( $\lambda_{irr} = 365$  nm, 30 min). The dots underneath the filled signals in (c) mark the signals univocally assigned to the species followed for the kinetic measurements: green: **1**·*E*-2<sup>+</sup>; orange: **1**·*Z*-2<sup>+</sup>; cyan: *Z*-2<sup>+</sup>; black: *E*-2<sup>+</sup>. Ratios in (b) and (c) indicate the complex associated fraction (complex:axle) obtained by integration of univocally identified, non-overlapping, signals for complex and free axle.

## 2.3 NMR Photochemistry

About 6 cm of the coating were removed from the terminal end of a quartz optical fiber (~5 m). The exposed quartz core was sanded in order to diffuse light into solution. In a typical NMR experiment, the exposed core of the fiber was immersed in 0.6 mL of an equimolar solution ( $\sim 9 \times 10^{-3}$  M) of *E-2*<sup>+</sup> and **1** inside an NMR tube. The other extremity of the fiber was connected to a LED apparatus equipped with two filter holders. The wavelength of emission was  $365 \pm 5$  nm, selected using a hard coated bandpass interference filter. The number of incident photons was selected using an additional neutral density (ND) filter with known optical density.

### 2.3.1 Optical Fiber Emission Spectra

The polychromatic emission spectra of the light source at different light intensities obtained with the appropriate neutral density filter consist of broad bands with a maximum at 369 nm (Fig. S2a). The  $365 \pm 5$  nm interference filter significantly narrowed the emission spectrum (Fig. S2b). In both setups, the integral of the emission bands, which is proportional to the output power, changes linearly with the transmittance of the ND filter (insets in Fig. S2). The emission spectra reported in Fig. S2b correspond to the “monochromatic” irradiation wavelength used in all the photochemical experiments.

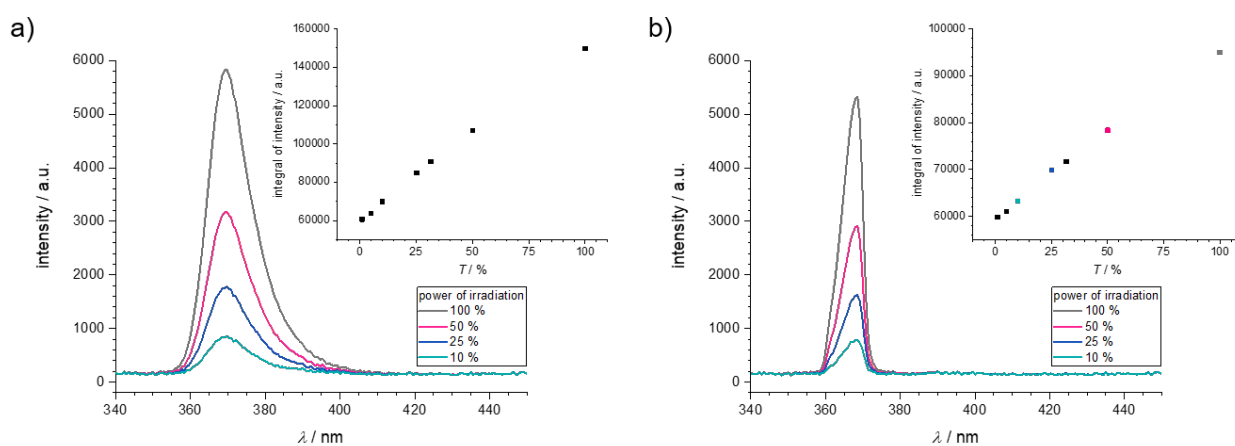


**Figure S2.** Emission spectra of the light source a) polychromatic setup b) monochromatic setup. In the inset the plot of integrated intensity on the percentage of transmitted light achieved with the appropriate ND filter. Light intensity values corresponding to those used for pump operation are reported in the same color as the corresponding spectrum in the inset.

### 2.3.2 NMR Chemical Actinometry

In order to estimate the photon flow of the optical fiber chemical actinometry was performed using the same experimental setup as for the molecular pump irradiation experiments using azobenzene as the actinometer. A solution of azobenzene in CD<sub>3</sub>OD ( $1.19 \times 10^{-2}$  M, 0.6 mL) was irradiated at 365 nm inside the NMR tube and *E*→*Z* isomerization was followed by <sup>1</sup>H NMR (Fig. S3). Photostationary state (PSS) was reached in about 50 min. The photon flow ( $q_{n,p}$ ) and the  $\epsilon_Z$  were

determined by least-square fitting of the concentration profiles of *E*- and *Z*-azobenzene to the photokinetic equation set (see below eq. S8 and S9), considering the thermal *Z*→*E* isomerization. Molar absorption coefficient for *E*-azobenzene<sup>2</sup> and quantum yields<sup>3</sup> in methanol were taken from literature data, while the obtained molar absorption coefficient for *Z*-azobenzene at 365 nm is in line with the reported data<sup>3</sup>. A photon flow ( $q_{n,p,max}$ ) of  $4.4 \times 10^{-8}$  Einstein s<sup>-1</sup> was obtained, corresponding to an output power of about 14 mW.

**Table S1.** Photophysical data of azobenzene in methanol used for actinometry.

$\varepsilon$ (M <sup>-1</sup> cm <sup>-1</sup> )		$\phi^{E-Z}$ [a]	$\phi^{Z-E}$ [a]	$k_{\Delta}$ (s <sup>-1</sup> )
<i>E</i> -azobenzene	<i>Z</i> -azobenzene			
375 <sup>[b]</sup>	92 <sup>[c]</sup>	0.12	0.34	$1.0 \times 10^{-6}$

<sup>[a]</sup>Ref. 3. <sup>[b]</sup>Ref. 2. <sup>[c]</sup>Fitted parameter.

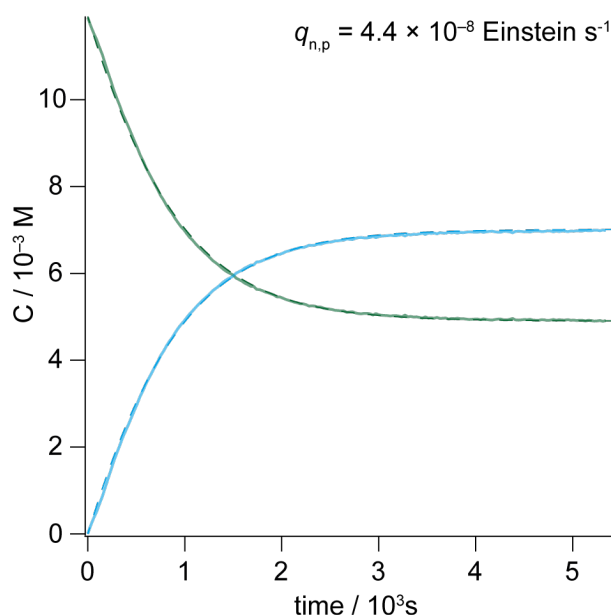


**Figure S3.** <sup>1</sup>H NMR kinetic of photoconversion of azobenzene ( $1.19 \times 10^{-2}$  M, CD<sub>3</sub>OD, 298 K). *E*-azobenzene: green line, *Z*-azobenzene: blue line. Solid lines represent the experimental concentration profile, dashed lines are least square fitting to the photokinetic equations set.

Since the radiant power increases linearly with the transmittance (Fig. S2), the number of incident photons for the numerical simulations (see below) was calculated from the 100% intensity diminished by the optical density of the filter used according to the following equation.

$$q_{n,p} = q_{n,p,max} \times 10^{-O.D.} \quad (S1)$$

### 3. Operation of the Supramolecular Pump

Typically, an equimolar mixture of **1** and  $E\text{-}2^+$  ( $\sim 9 \times 10^{-3}$  M) was allowed to reach thermodynamic equilibrium in the dark, then a non-equilibrium mixture of  $Z$  axle and  $Z$  complex was obtained by photoisomerization of the azobenzene unit. Photoisomerization was performed *in situ* using the setup described in section 2.3.

Upon reaching a stable  $Z/E$  composition (PSS) irradiation was interrupted (Fig. S4, black trace) or reduced (Fig. S4, colored traces) and the time-dependent changes in concentration of the photoactive species were followed by  $^1\text{H}$  NMR.

The initial concentrations of **1** and  $E\text{-}2^+$  used in each experiment are reported in Table S2.

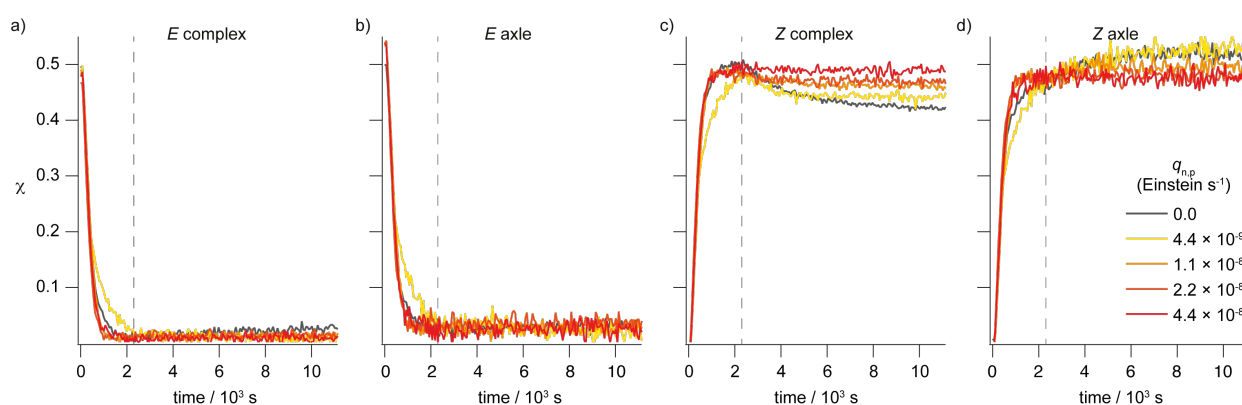
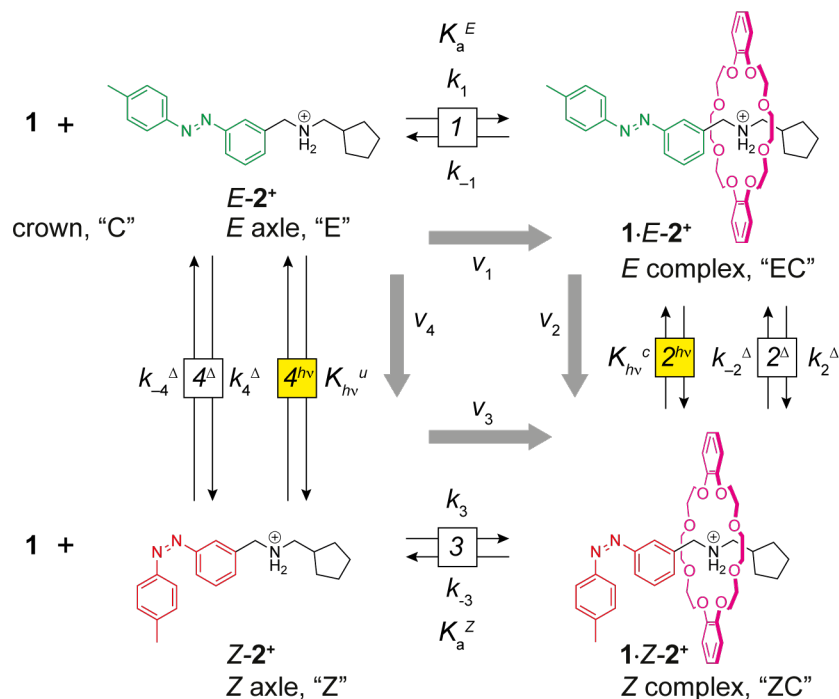


**Figure S4.** Time-dependent molar fraction profiles of  $E$  complex (a),  $E$  axle (b),  $Z$  complex (c), and  $Z$  axle (d) at different light intensities generated by light-induced isomerization of an equilibrated mixture of  $E\text{-}2^+$  and **1**. The gray dashed line indicates the time at which PSS is reached. Data obtained from  $^1\text{H}$  NMR data (500 MHz,  $\text{CD}_3\text{CN}$ , 298 K, initial concentrations for each experiment are reported in Table S2).

**Table S2.** Experimental initial concentrations of **1** and  $E\text{-}2^+$ .

$q_{n,p}$ (Einstein $\text{s}^{-1}$ )	0	$4.4 \times 10^{-9}$	$1.1 \times 10^{-8}$	$2.2 \times 10^{-8}$	$4.4 \times 10^{-8}$
(% of $q_{n,p,max}$ )	0%	10%	25%	50%	100%
$[2^+]_0$ (M)	$8.91 \times 10^{-3}$	$7.43 \times 10^{-3}$	$7.43 \times 10^{-3}$	$7.43 \times 10^{-3}$	$8.17 \times 10^{-3}$
$[1]_0$ (M)	$8.98 \times 10^{-3}$	$7.48 \times 10^{-3}$	$7.48 \times 10^{-3}$	$7.48 \times 10^{-3}$	$8.23 \times 10^{-3}$

The complete closed reaction network describing the pumping cycle for compounds **1** and **2<sup>+</sup>** is reported in Scheme S1. This set of six reactions (four thermal and two photochemical) was implemented in appropriate kinetic models for fitting or simulating the experimental data (see section 4).



**Scheme S1.** Complete reaction network for compound **2<sup>+</sup>** and **1** used to fit and simulate the experimental behavior. Reactions are numbered clockwise starting from the top. “ $K$ ” and “ $k$ ” indicate equilibrium and rate constants respectively. “ $h\nu$ ” and “ $\Delta$ ” indicate the photochemical and thermal ( $E \rightarrow Z$  and  $Z \rightarrow E$ ) isomerization processes respectively. Conventionally, the rates of reaction are positive for the reaction read from left to right and from top to bottom (gray arrows).

### 3.1 Cycling Rate

Under light irradiation, at the steady state the rates of all reactions must be equal in magnitude and their value corresponds to the cycling rate. The rate of reaction 3 was determined using the appropriate rate law (equation 1 of the manuscript) and the experimental concentration of complex, axle, and macrocycle. The steady state rates reported in the manuscript were measured by averaging the rate values over the last 15 minutes.



### 3.2 Cycle Quantum Yield

The cycle quantum yield ( $\Phi_{cy}$ ) represents the number of cycles performed in a given interval of time divided by the corresponding number of photons absorbed in the same time interval (equation S2). The number of moles of photons absorbed by the system per unit time was determined from the photons emitted by the light source considering the absorbance of the solution at 365 nm (section 2.2). The number of moles of pumps that completed a cycle in a given time is equal to the rate of cycling multiplied by the time interval and by the volume of the irradiated solution. The rate of cycling at steady state was measured from the rate of reaction 3 (section 3.1).

$$\Phi_{cy} = \frac{N_{cycles}}{N_{ph,abs}} = \frac{v_{cycling} \times \Delta t \times V}{q_{n,p}(1-10^{-A}) \times \Delta t} \quad (S2)$$

### 3.3 Kinetic Asymmetry

With reference to Scheme S1, the kinetic asymmetry (ratcheting constant,  $K_r$ ) of the cycle can be rigorously quantified as:<sup>4</sup>

$$K_r = \frac{r_1 r_2 r_{-3} r_{-4}}{r_{-1} r_{-2} r_3 r_4} \quad (S3)$$

where,  $r_i$  and  $r_{-i}$  are the rates of the  $i$ -th process forward and backward respectively. Since the reactions describe a closed cycle and considering that the rate for processes 2 and 4 is the sum of the photochemical and thermal reaction rates ( $r_i = r_i^{hv} + r_i^{\Delta}$ ),  $K_r$  can also be written in terms of the rate constants of the processes reported in Scheme S1:

$$K_r = \frac{k_1(k_2^{hv} + k_2^{\Delta})k_{-3}(k_4^{hv} + k_4^{\Delta})}{k_{-1}(k_{-2}^{hv} + k_{-2}^{\Delta})k_3(k_4^{hv} + k_4^{\Delta})} = K_a^E \frac{F_{hv}\epsilon_{EC}\phi_{EC} + k_2^{\Delta}}{F_{hv}\epsilon_{ZC}\phi_{ZC} + k_{-2}^{\Delta}} (K_a^Z)^{-1} \frac{F_{hv}\epsilon_Z\phi_Z + k_{-4}^{\Delta}}{F_{hv}\epsilon_E\phi_E + k_4^{\Delta}}$$

Where  $F_{hv} = \frac{q_{n,p} \cdot b \cdot (1-10^{-A})}{V \cdot A}$  and  $A = b \cdot \sum_i \epsilon_i \cdot [i]$ .

In the dark ( $q_{n,p} = 0$ )  $F_{hv}$  is null and  $K_r = 1$  due to the microscopic reversibility of the thermal processes.<sup>5</sup> Conversely, in case of irradiation ( $q_{n,p} > 0$ ), the kinetic constants for thermal isomerization reactions (indicated with a “ $\Delta$ ” superscript) can be neglected with respect to the photochemical ones. As a result, the light-dependent parts of the equation simplify to the photostationary state composition for axle and complex. Moreover, for the present system is fair to assume that these are equally populated ( $K_{hv}^u = K_{hv}^c$ ) and therefore:

$$K_r \approx K_a^E \frac{\epsilon_{EC}\phi_{EC}}{\epsilon_{ZC}\phi_{ZC}} (K_a^Z)^{-1} \frac{\epsilon_Z\phi_Z}{\epsilon_E\phi_E} = K_a^E K_{hv}^c (K_a^Z)^{-1} (K_{hv}^u)^{-1} \approx \frac{K_a^E}{K_a^Z} = 2$$

In Table S3 are reported the absolute rates of reaction for all processes obtained from numerical simulations (see section 4.2) and the ratcheting constants at different photon flows calculated using equation S3.

**Table S3.** Computed forward and backward reaction rates obtained from numerical simulations and calculated ratcheting constants.

	<b><math>q_{n,p}</math> (Einstein <math>s^{-1}</math>)</b>	$4.4 \times 10^{-9}$	$1.1 \times 10^{-8}$	$2.2 \times 10^{-8}$	$4.4 \times 10^{-8}$
thermal reactions	<b><math>r_1</math> (<math>10^{-6}</math> M <math>s^{-1}</math>)</b>	5.70	5.34	5.33	5.90
	<b><math>r_{-1}</math> (<math>10^{-6}</math> M <math>s^{-1}</math>)</b>	5.65	5.24	5.16	5.59
	<b><math>r_3</math> (<math>10^{-6}</math> M <math>s^{-1}</math>)</b>	0.625	0.575	0.526	0.599
	<b><math>r_{-3}</math> (<math>10^{-6}</math> M <math>s^{-1}</math>)</b>	0.676	0.679	0.692	0.906
photoreactions	<b><math>r_2</math> (<math>10^{-6}</math> M <math>s^{-1}</math>)</b>	0.213	0.497	0.979	2.09
	<b><math>r_{-2}</math> (<math>10^{-6}</math> M <math>s^{-1}</math>)</b>	0.147	0.378	0.797	1.77
	<b><math>r_4</math> (<math>10^{-6}</math> M <math>s^{-1}</math>)</b>	0.192	0.470	0.952	1.99
	<b><math>r_{-4}</math> (<math>10^{-6}</math> M <math>s^{-1}</math>)</b>	0.234	0.566	1.11	2.29
	<b><math>K_r^{[a]}</math></b>	1.9	1.9	2.0	2.2

<sup>[a]</sup>Calculated using equation S3 from computed reaction rates.

## 4. Fitting and Numerical Simulations

### 4.1 Fitting of the dethreading kinetic

Second order threading rate constant ( $k_{in}^E = k_1$ ) and equilibrium constant ( $K_a^E$ ) for the *E* isomer were determined independently by UV-Vis and  $^1\text{H}$  NMR.<sup>1</sup> The rate constant of dethreading of compound  $Z\text{-}2^+$  ( $k_{-3}$ ) was determined by fitting of the time-dependent concentration profiles of *Z* axle and *Z* complex reaching the local according to a kinetic model including the thermal reactions of Scheme S1. The average value obtained from four independent “relaxation” experiments (black trace in figure S4) is  $(2.3 \pm 0.4) \times 10^{-4} \text{ s}^{-1}$ , which is in excellent agreement with the previously reported data (Table S4) and was used in all the following calculations.

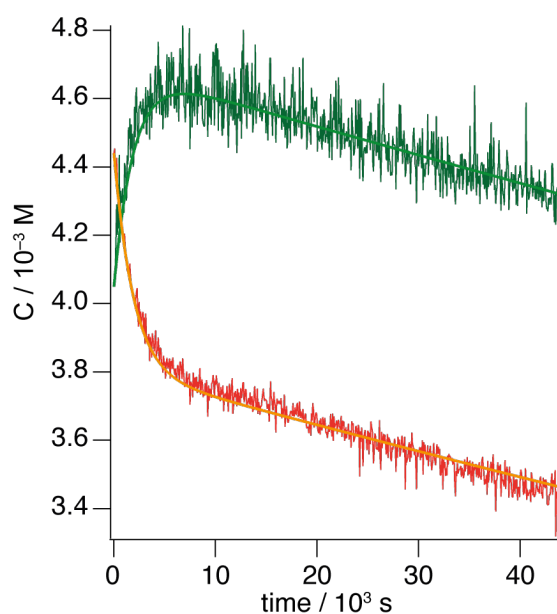


**Figure S5.** Typical kinetic of equilibration of a mixture of  $Z\text{-}2^+$  and **1**, generated by fast light-induced isomerization of the corresponding equilibrated mixture of  $E\text{-}2^+$  and **1**. Data obtained from  $^1\text{H}$  NMR measurements (500 MHz,  $\text{CD}_3\text{CN}$ , 298 K). *Z* complex: red trace; *Z* axle: green trace. Solid lines represent the least square fitting according to the thermal reactions of scheme S1. Conditions:  $\text{CD}_3\text{CN}$ ,  $C = 8.9 \text{ mM}$ , 298 K.

**Table S4.** Comprehensive table of the experimental thermodynamic, kinetic, photophysical, and photochemical parameters for axle  $E\text{-}2^+$ ,  $Z\text{-}2^+$ , and for the corresponding [2]pseudorotaxane in air-equilibrated  $\text{CH}_3\text{CN}$ .<sup>[a]</sup>

	$K_a$ ( $\text{M}^{-1}$ )	$k_{\text{in}}$ ( $\text{M}^{-1} \text{s}^{-1}$ )	$k_{\text{out}}$ ( $\text{s}^{-1}$ )	$k_{\Delta}$ ( $\text{s}^{-1}$ )	$\phi$ <sup>[b]</sup>	$\epsilon_{365}$ ( $\text{M}^{-1} \text{cm}^{-1}$ )
$E\text{-}2^+$	[c]	[c]	[c]	[c]	0.23 ( $E \rightarrow Z$ )	3900
$Z\text{-}2^+$	[c]	[c]	[c]	$1.9 \times 10^{-6}$	0.58 ( $Z \rightarrow E$ )	< 100
$1 \cdot E\text{-}2^+$	$230 \pm 30$	$16$ <sup>[d]</sup>	$0.07$ <sup>[e]</sup>	[c]	0.22 ( $E \rightarrow Z$ )	4800
$1 \cdot Z\text{-}2^+$	$170 \pm 30$ $115 \pm 35$ <sup>[f]</sup>	$3.1 \pm 0.8 \times 10^{-2}$ <sup>[g]</sup>	$2.7 \pm 0.5 \times 10^{-4}$ <sup>[g]</sup> $2.3 \pm 0.4 \times 10^{-4}$ <sup>[h]</sup>	$4.8 \times 10^{-6}$	0.59 ( $Z \rightarrow E$ )	< 100

<sup>[a]</sup>Data reported in ref. 1. *Italicized* values were newly determined in this work. <sup>[b]</sup>Determined at 365 nm. The corresponding isomerization process is given in brackets. <sup>[c]</sup>Parameter is not relevant for the compound. <sup>[d]</sup>Determined by stopped-flow UV-Vis absorption method. <sup>[e]</sup>Calculated as  $k_{\text{in}}/K_a$ . <sup>[f]</sup>Calculated as  $k_{\text{in}}/k_{\text{out}}$ . <sup>[g]</sup>Determined by non-linear regression of the time-dependent  $^1\text{H}$  NMR concentration profiles. <sup>[h]</sup>Same as (g) but determined in *this work* by regression of the dethreading kinetic. This value was used as the basis for the  $k_{-3}$  in the numerical simulations (see table S4).

## 4.2 Numerical Simulations

The kinetic behavior of the reaction network was simulated taking into consideration all the thermal and photochemical reactions in scheme S1. The reaction rates for all processes were computed separately at any point in time solving the linear system of differential equations (S4 to S8) that defines the pumping cycle with a stiff ODE solver (ode15s).

Concerning the implementation, the linear system describing the pumping cycle is time-variant (LTV), therefore simulations were carried out considering three time-invariant steps (LTI): a) equilibration, b) photoisomerization, and c) operation regime. The solutions from the previous LTI were taken as initial conditions for the subsequent one. The system is assumed to be in well-mixed conditions. Thus, diffusion of species is never considered rate limiting and all concentrations used in the rate laws are homogeneous in space. Details for the three steps are given below:

- First the macrocycle and  $E$ -axle association in the dark was simulated using the initial experimental concentrations of  $E\text{-}2^+$  and  $1$  as initial conditions for the numerical solution. A photon flow of  $0.0 \text{ Einstein s}^{-1}$  ("light off") was set in this step (photochemical rates are neglected). A close match between the simulated and experimental equilibrium composition in the dark was obtained.
- Starting from these equilibrium concentrations of  $E$  axle and  $E$  complex the isomerization was simulated using the photokinetic equations (eq. S8). In this step the photon flow was set to the value of  $4.4 \times 10^{-8} \text{ Einstein s}^{-1}$  for about 35 min, consistently with the experimental

procedure. Pleasingly, the simulated PSS concentrations (>95% conversion to Z isomers) matched very closely the experimental ones (Fig. S6) validating this methodology of simulation and the actinometry results (section 2.3).

- c) Finally, from the simulated PSS concentrations the photon flow was set to the actual experimental value, and the system was allowed to reach the local equilibrium state or the kinetic steady state respectively in absence or presence of the light. Five possible photon flows ranging from 0.0 to  $4.4 \times 10^{-8}$  Einstein  $s^{-1}$  were used in the simulations in line with the experiments.

The rates of thermal reactions (1,3,  $2^\Delta$ , and  $4^\Delta$ ) were computed with the corresponding rate equations (S4 to S7). The rate constants of reaction 3 were adjusted within the experimental error to achieve the best overlay with the experimental concentration profiles (table S4). The rate constants for the thermal  $E \rightarrow Z$  isomerization reactions ( $k_2^\Delta$  and  $k_4^\Delta$ ), included in Scheme 1 for completeness, were neglected in the simulations. As a result, reactions  $2^\Delta$  and  $4^\Delta$  appear as unidirectional processes that convert Z isomers to the corresponding E form (equations S6 and S7).

$$\text{Reaction 1:} \quad v_1 = k_1[E \text{ axle}][\mathbf{1}] - k_{-1}[E \text{ complex}] \quad (\text{S4})$$

$$\text{Reaction 3:} \quad v_3 = k_3[Z \text{ axle}][\mathbf{1}] - k_{-3}[Z \text{ complex}] \quad (\text{S5})$$

$$\text{Reaction } 2^\Delta: \quad v_{2\Delta} = k_2^\Delta[Z \text{ complex}] \quad (\text{S6})$$

$$\text{Reaction } 4^\Delta: \quad v_{4\Delta} = k_4^\Delta[Z \text{ axle}] \quad (\text{S7})$$

Where the  $\Delta$  superscripts refer to the thermal  $Z \rightarrow E$  isomerization process.

Rates of  $E \rightarrow Z$  and  $Z \rightarrow E$  photochemical isomerization for the free and complexed axles (reactions  $2^{hv}$  and  $4^{hv}$ ) were calculated using the photokinetic rate law (S8). Experimental quantum yields ( $\phi$ ) and molar absorption coefficients ( $\epsilon$ ) determined at 365 nm, as well as the photon flow determined by chemical actinometry ( $q_{n,p,max}$ ) were used. The absorbance of the mixture at the irradiation wavelength ( $A_{TOT}$ ) was calculated according to Beer-Lambert's law at any point in time from the calculated mixture composition. Equation S8 is the general photokinetics equation<sup>6</sup> for the photoisomerization of the  $i$ -th species ( $i = E \text{ axle}, Z \text{ axle}, E \text{ complex}, Z \text{ complex}$ ).

$$v_i = \frac{q_{n,p} \cdot b}{V} \cdot \phi^i \cdot \epsilon_i \cdot [i] \frac{1 - 10^{-A_{TOT}}}{A_{TOT}} \quad (\text{S8})$$

It must be noted that each photoactive species needs two photokinetic rate laws accounting for both  $E \rightarrow Z$  and  $Z \rightarrow E$  photochemical isomerization processes.

A total of four photokinetic equations plus the six rate laws are needed to appropriately simulate the pumping cycle (Scheme S1). In Fig. S6 (top row) the simulated concentration profiles of all the

photoactive species are displayed. In table S5 the parameters used in the dynamic simulations reported in Fig. 3 of the main text and Fig. S6 are reported.

**Table S5.** Experimental initial concentrations of **1** and  $E\text{-}2^+$ , rate constants, and photophysical parameters used for the numerical simulations at the different photon flows.<sup>[a]</sup>

$q_{n,p}$ (Einstein $s^{-1}$ )	0	$4.4 \times 10^{-9}$	$1.1 \times 10^{-8}$	$2.2 \times 10^{-8}$	$4.4 \times 10^{-8}$
(% of $q_{n,p,max}$ )	0%	10%	25%	50%	100%
$[2^+]_0$ (M) <sup>[b]</sup>	$8.91 \times 10^{-3}$	$7.43 \times 10^{-3}$	$7.43 \times 10^{-3}$	$7.43 \times 10^{-3}$	$8.17 \times 10^{-3}$
$[1]_0$ (M) <sup>[b]</sup>	$8.98 \times 10^{-3}$	$7.48 \times 10^{-3}$	$7.48 \times 10^{-3}$	$7.48 \times 10^{-3}$	$8.23 \times 10^{-3}$
$k_3$ ( $M^{-1} s^{-1}$ ) <sup>[c]</sup>	$3.65 \times 10^{-2}$	$3.7 \times 10^{-2}$	$3.7 \times 10^{-2}$	$3.5 \times 10^{-2}$	$3.65 \times 10^{-2}$
$k_{-3}$ ( $s^{-1}$ ) <sup>[d]</sup>	$2.25 \times 10^{-4}$	$2.1 \times 10^{-4}$	$2.0 \times 10^{-4}$	$2.0 \times 10^{-4}$	$2.25 \times 10^{-4}$
$\varepsilon_{EC}$	4800	4800	4800	4800	4800
$\varepsilon_E$	3900	3900	3900	3900	3900
$\varepsilon_{ZC}$ <sup>[e]</sup>	30	31	30	31	30
$\varepsilon_Z$ <sup>[e]</sup>	40	40	40	40	40
$\phi^{E \rightarrow Z}$	0.23	0.23	0.23	0.23	0.23
$\phi^{Z \rightarrow E}$	0.58	0.58	0.58	0.58	0.58
$\phi^{EC \rightarrow ZC}$	0.22	0.22	0.22	0.22	0.22
$\phi^{ZC \rightarrow EC}$	0.59	0.59	0.59	0.59	0.59

<sup>[a]</sup>The parameters shaded in orange were adapted within the confidence interval of the experimental value to achieve a better overlay with the data. <sup>[b]</sup>Experimental concentration. <sup>[c]</sup>Adapted in the interval  $(3.1 \pm 0.8) \times 10^{-4} M^{-1} s^{-1}$ . <sup>[d]</sup>Adapted in the interval  $(2.3 \pm 0.4) \times 10^{-4} s^{-1}$ . <sup>[e]</sup>Value calculated in order for the ratio  $\frac{\phi^{EZ}\varepsilon_E}{\phi^{ZE}\varepsilon_Z}$  to match the experimental composition at the PSS; minor modifications were performed to achieve a better overlay with the experimental data.

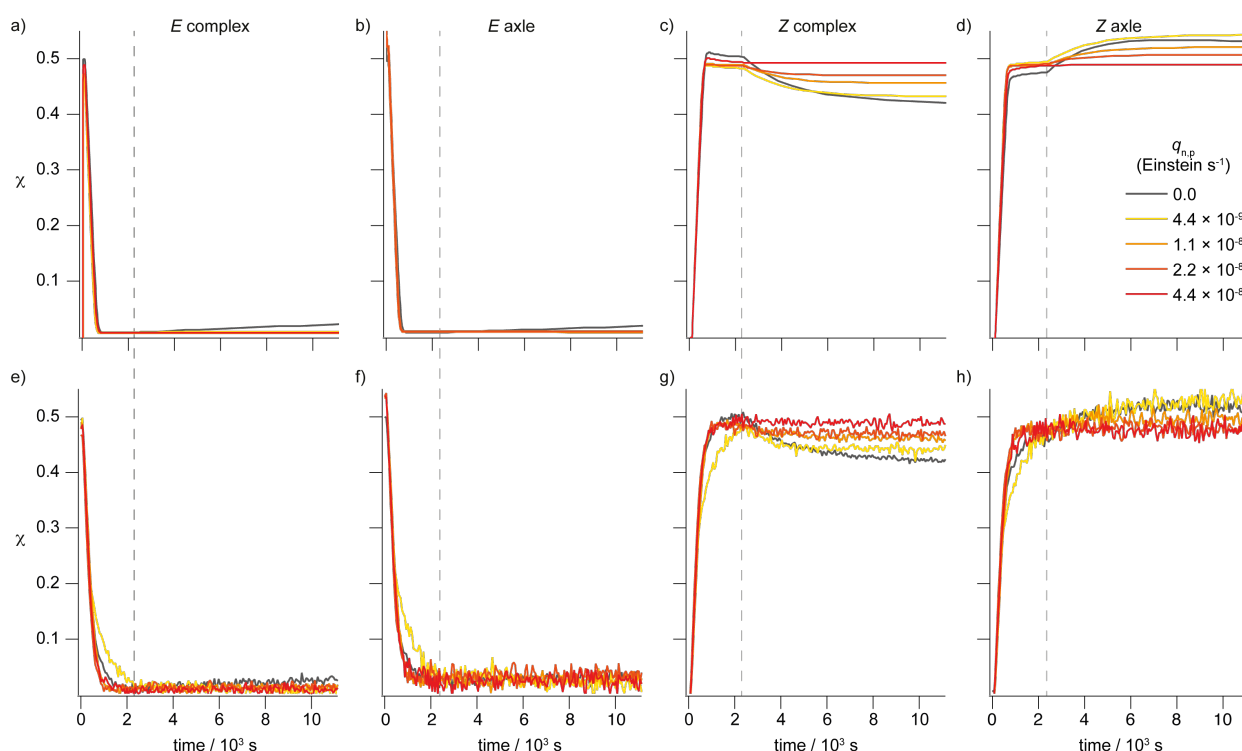


**Figure S6.** Simulated molar fraction profiles (top row) at different light intensities of all species generated by light-induced isomerization of an equilibrated mixture of *E*-**2**<sup>+</sup> and **1**. On the bottom row the corresponding experimental profiles (Fig. S4) are reported for comparison. *E* complex (a, e), *E* axle (b, f), *Z* complex (c, g), and *Z* axle (d, h). The gray dashed line indicates the time at which PSS is reached. Data obtained from <sup>1</sup>H NMR data (500 MHz, CD<sub>3</sub>CN, 298 K, initial concentrations for each experiment are reported in Table S4).

## 5. Thermodynamic Analysis

All the following thermodynamic considerations are made in the steady state regime, unless otherwise specified, that is, analogously to equilibrium condition, time-invariant. The steady state concentrations of all species extracted from time-dependent <sup>1</sup>H NMR experiments are reported in table S6.

**Table S6.** Experimental and simulated molar concentrations of **1**, *E*-**2**<sup>+</sup>, *Z*-**2**<sup>+</sup> and of the corresponding complexes at the local equilibrium (dark) or dissipative steady states (light on).

	$q_{n,p}$ (Einstein s <sup>-1</sup> )				
	Dark	$4.4 \times 10^{-9}$	$1.1 \times 10^{-8}$	$2.2 \times 10^{-8}$	$4.4 \times 10^{-8}$
[EC] (M) <sup>[a]</sup>	$2.24 \times 10^{-4}$	$8.07 \times 10^{-5}$	$7.48 \times 10^{-5}$	$7.34 \times 10^{-5}$	$7.99 \times 10^{-5}$
[E] (M) <sup>[a]</sup>	$2.00 \times 10^{-4}$	$8.53 \times 10^{-5}$	$8.32 \times 10^{-5}$	$8.46 \times 10^{-5}$	$9.01 \times 10^{-5}$
[ZC] (M) <sup>[b]</sup>	$3.76 \times 10^{-3}$	$3.28 \times 10^{-3}$	$3.42 \times 10^{-3}$	$3.49 \times 10^{-3}$	$4.00 \times 10^{-3}$
[Z] (M) <sup>[b]</sup>	$4.59 \times 10^{-3}$	$3.96 \times 10^{-3}$	$3.69 \times 10^{-3}$	$3.57 \times 10^{-3}$	$3.91 \times 10^{-3}$
[C] (M) <sup>[c]</sup>	$4.95 \times 10^{-3}$	$4.13 \times 10^{-3}$	$3.94 \times 10^{-3}$	$3.86 \times 10^{-3}$	$4.13 \times 10^{-3}$

<sup>[a]</sup>Determined from dynamics simulation. <sup>[b]</sup>Experimental molar concentrations calculated from the mole fractions (observable) averaged over the last 15 min and the initial concentration of axle. <sup>[c]</sup>Determined applying mass balance considerations.

## 5.1 Chemical Potential of Reaction

The non-standard chemical potential of reaction (also known as thermodynamic affinity when taken with a minus sign) was calculated from the concentrations maintained at the kinetic steady state away from equilibrium according to equation S9.<sup>7</sup> At any point along the reaction coordinate the  $\Delta\mu$  is given by the sum of the chemical potential of each species ( $\mu_i$ ) multiplied by the corresponding stoichiometric coefficient (negative for reagents). In particular, a positive value of  $\Delta\mu$  corresponds to a steady state shifted towards the products ( $\mu_P > \mu_R$ ), while the opposite holds for a negative  $\Delta\mu$ . For a generic reaction of the kind  $A + B \rightarrow P$  the overall variation in chemical potential thus reads:

$$\Delta\mu = -\mu_A - \mu_B + \mu_P$$

Then:

$$\Delta\mu = -\mu_A^0 - RT \ln[A] - \mu_B^0 - RT \ln[B] + \mu_P^0 + RT \ln[P] = \underbrace{-\mu_A^0 - \mu_B^0 + \mu_P^0}_{\Delta\mu^0} + RT \ln \frac{[P]}{[A][B]}$$

$$\Delta\mu = RT \ln Q - RT \ln K \quad (\text{S9})$$

where  $K$  is the equilibrium constant of the reaction,  $Q$  is the reaction quotient. The sum of the non-standard chemical potential (thermodynamic affinities when taken with the opposite sign) along the cycle of scheme S1 is the free energy dissipated along one cycle of operation.

## 5.2 Thermodynamic of Radiation

Fig. S7a and b present a scheme of the irradiation setup used in this study, which served as the basis for the thermodynamic analysis. The first step of our thermodynamic analysis is to determine the concentration of photons in a volume element  $dV_{cyl}(r)$  consisting of an infinitesimally thin cylindrical shell of thickness  $dr$  (inner radius  $r$  and outer radius  $r + dr$ ) axial to the optical fiber and the NMR tube (highlighted in red Fig. S7c). The volume of the cylindrical shell is  $dV_{cyl}(r) = \pi h((r + dr)^2 - r^2) = 2\pi h r dr$ .

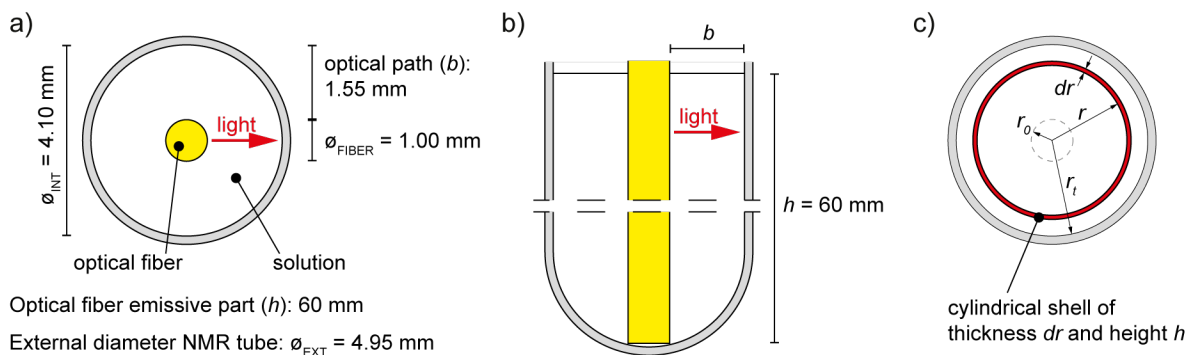


**Figure S7.** Scheme of the optical geometry and dimensions of the irradiation setup. a) Top view. b) Side view. c) Modelling of the infinitesimal volume travelled by light in a unit time used in the thermodynamic analysis ( $r_0 = 0.5$  mm,  $r_t = \varnothing_{INT}/2 = 2.05$  mm).



The moles of photons in this volume ( $dN_{hv}(r)$ ) can be computed by multiplying the number of moles of photons impinging on the inner surface per unit time ( $q_{n,p}(r)$ ) by the time that light takes to travel the distance  $dr$  ( $t = dr/c$ , where “c” is the speed of light):

$$dN_{hv}(r) = q_{n,p}(r) \cdot t = \frac{q_{n,p}(r)}{c} dr$$

The molar concentration of photons in the volume  $dV_{cyl}(r)$  is then:

$$n_{hv}(r) = \frac{dN_{hv}(r)}{dV_{cyl}(r)} = \frac{q_{n,p}(r)}{2\pi hcr} = \frac{q_{n,p}}{2\pi hc} \cdot \frac{10^{-(r-r_0) \sum_i \varepsilon_i [i]}}{r}$$

where the dependence of  $q_{n,p}(r)$  on  $r$  has been expressed in terms of the Beer-Lambert's law and the total amount of photons emitted by the optical fiber ( $q_{n,p}(r_0) \equiv q_{n,p}$ ). It is worth noting that the molar concentration of photons in the volume  $dV_{cyl}(r)$  has, in principle, also a contribution  $n_{bb}^T$  (constant along  $r$ ) from the black body emission of the solution due to its temperature  $T$ . However, such a contribution is negligible at any  $r$  when compared to that of the source at the wavelength and intensity considered.

To proceed with our analysis, we now define the effective temperature  $T_{hv}(r)$  associated with the radiation in the volume  $dV_{cyl}(r)$ . Such a temperature is the one that a black body needs to have in order to generate a molar concentration of photons equal to  $n_{hv}(r)$  in the interval selected by the interference filter (365±5 nm), and can be computed by solving numerically the following equation:

$$n_{hv}(r) = \int_{360 \text{ nm}}^{370 \text{ nm}} n_{bb}(\lambda) d\lambda = \int_{360 \text{ nm}}^{370 \text{ nm}} \frac{8\pi}{N_A \lambda^4} \cdot \frac{1}{e^{hc/\lambda k_B T_{hv}} - 1} d\lambda$$

where  $N_A$  is the Avogadro's number,  $h$  the Planck's constant, and  $k_B$  the Boltzmann's constant. The above equation uniquely defines  $T_{hv}(r)$  and is well justified within the monochromatic assumption. Indeed, as all the photons impinging on the system are considered at the same frequency, the exact shape of their distribution in frequency in the interval selected by the interference filter has no role in the treatment, and can therefore be assumed to be the black body one ( $n_{bb}(\lambda)$ ) without altering the final results. This has the major advantage that the radiation in the volume  $dV_{cyl}(r)$  can be considered as a heat source at temperature  $T_{hv}(r)$ . Since the solvent acts as another heat source at temperature  $T$ , we can properly think of the molecular motor as a

thermal engine working by virtue of the temperature gradient between the radiation and the solvent. As a consequence, we can immediately conclude that the maximum efficiency at which the motor can convert the energy absorbed from the radiation into work in the volume  $dV_{cyl}(r)$  is limited by Carnot's theorem:

$$\eta_C(r) = 1 - \frac{T}{T_{hv}(r)}$$

We can have a first idea of the thermodynamics of the motor by computing the average temperature of the radiation and the average Carnot's efficiency (Table S7).

$$\langle T_{hv} \rangle = \frac{1}{b} \int_{r_0}^{r_t} T_{hv}(r) dr$$

$$\langle \eta_C \rangle = \frac{1}{b} \int_{r_0}^{r_t} \eta_C(r) dr$$

Note that, by virtue of the inequality holding between the harmonic mean and the arithmetic mean of a positive defined function, we have that:

$$\langle \eta_C \rangle = 1 - T \left\langle \frac{1}{T_{hv}} \right\rangle \leq 1 - \frac{T}{\langle T_{hv} \rangle}$$

and therefore the Carnot's efficiency computed by using the average temperature of the hot heat source ( $\langle T_{hv} \rangle$ ) provides an upper bound to the maximum efficiency of the whole system considered as a thermal engine.

To have further quantitative insights on the thermodynamic characterization of the system, we introduce the chemical potential of the radiation as:<sup>8</sup>

$$\mu_{hv}(r) = N_A h\nu \cdot \eta_C(r)$$

In this context, the chemical potential of the radiation can be interpreted as the part of the molar energy coming from the light source which is actually available to the system in the volume  $dV_{cyl}(r)$  (the free energy in the volume). It is also the amount of energy which can be used to take the system away from thermodynamic equilibrium by performing work on it. From the above expression, whenever the concentration of photons in the volume  $dV_{cyl}(r)$  is such that  $T_{hv}(r) = T$ , with a molar concentration of photons equal to  $n_{bb}^T$ , corresponding to the black body emission of the solution at the temperature  $T$ , the chemical potential of the radiation is null. Therefore, the radiation cannot perform any work on the system in that volume element. In this condition which

corresponds to the absence of radiation from the source the only possible steady state for the system is the equilibrium one. In Table S7, the average chemical potential for the five experimental regimes is reported. The average chemical potential of the radiation in the system is way larger than the thermal energy ( $RT$ ) and about one order of magnitude higher than the free energy released upon hydrolysis of ATP to ADP in physiological conditions. Moreover, by increasing the light intensity, the average chemical potential of the radiation also increases, consistently with the system being brought farther away from equilibrium at higher photon fluxes.

**Table S7.** Average temperature of radiation ( $\langle T_{hv} \rangle$ ), Carnot's efficiency ( $\langle \eta_c \rangle$ ), and chemical potential of radiation ( $\langle \mu_{hv} \rangle$ ) at the investigated photon flows.<sup>[a]</sup>

$q_{n,p}$ (Einstein s <sup>-1</sup> )	$\langle T_{hv} \rangle$ (K)	$\langle \eta_c \rangle$	$\langle \mu_{hv} \rangle$ (kJ mol <sup>-1</sup> ) <sup>[a]</sup>
0	298	0	0 <sup>[b]</sup>
$4.4 \times 10^{-9}$	1917	0.844	277
$1.1 \times 10^{-8}$	2007	0.851	279
$2.2 \times 10^{-8}$	2081	0.857	281
$4.4 \times 10^{-8}$	2159	0.862	282

<sup>[a]</sup>The energy of one mole of 365 nm photons was estimated as  $N_A h\nu = 328$  kJ mol<sup>-1</sup>. <sup>[b]</sup>The actual value of photon flow at which the force is null is not 0 Einstein s<sup>-1</sup>, but rather a very small value of photon flow corresponding to a black body at 298 K emitting around 365 nm.

### 5.3 Energy Dissipation and Storage

We now couple the thermodynamic description with the system's kinetics. The number of moles of photons absorbed by the system per unit of time in the volume element  $dV_{cyl}(r)$  is:

$$\begin{aligned}
 dq_{n,p}(r) &= q_{n,p}(r) - q_{n,p}(r + dr) = q_{n,p}(r)(1 - 10^{-dr \sum_i \varepsilon_i [i]}) \\
 &= q_{n,p}(r) \sum_i \varepsilon_i [i] dr + \mathcal{O}(dr^2) \\
 &\approx q_{n,p}(r) \sum_i \varepsilon_i [i] dr
 \end{aligned}$$

from which we can compute the free energy absorbed by the system per unit of time ( $\dot{W}$ ) in the same volume element as:

$$d\dot{W}(r) = \mu_{hv}(r) dq_{n,p}(r) = \mu_{hv}(r) q_{n,p}(r) \sum_i \varepsilon_i [i] dr$$

However, since the quantum yield of photoisomerization is not unitary for the considered processes, the actual amount of absorbed free energy which can perform work on the system, thus modifying the species concentrations, is:

$$d\dot{W}_{hv}(r) = \mu_{hv}(r)q_{n,p}(r) \sum_i \phi_i \varepsilon_i [i] dr$$

Were the quantum yields ( $\phi_i$ ) are included to account for the amount of absorbed free energy which is unavoidably dissipated without leading to photoisomerization.

The integral of  $d\dot{W}_{hv}(r)$  over the space occupied by the solution and divided by the volume yields the input power of the molecular motor which appears in equation (2) of the main text, that is the work performed on the system by the radiation:

$$\dot{W}_{hv} = \frac{1}{V} \sum_i \phi_i \varepsilon_i [i] q_{n,p} \int_{r_0}^{r_t} \mu_{hv}(r) 10^{-(r-r_0) \sum_i \varepsilon_i [i]} dr$$

At any time, the free energy absorbed per unit time and volume can either be dissipated or stored in the system as free energy. This is expressed by equation (2) of the main text:

$$\dot{W}_{hv} = d_t G + T\dot{\Sigma}$$

where the dissipation rate per unit of volume is always positive ( $T\dot{\Sigma} \geq 0$ ) according to the second law of thermodynamics. Both the dissipation rate and the time derivative of the Gibbs free energy can be split into two contributions, one due to the isomerization steps ( $T\dot{\Sigma}_{iso}$ ), and the other to the self-assembly steps ( $T\dot{\Sigma}_{sa}$ ):

$$\begin{aligned} T\dot{\Sigma} &= T\dot{\Sigma}_{sa} + T\dot{\Sigma}_{iso} \\ d_t G &= d_t G_{sa} + d_t G_{iso} \end{aligned}$$

### 5.3.1 Energy dissipation

The part of the absorbed power which is dissipated by the self-assembly steps is calculated as:

$$T\dot{\Sigma}_{sa} = -(v_1 \Delta\mu_1 + v_3 \Delta\mu_3)$$

At the stationary state, since the Gibbs free energy is a state function, all the power absorbed by system is dissipated to sustain the non-equilibrium condition ( $d_t G = 0$ ):

$$\dot{W}_{hv} = T\dot{\Sigma} = T\dot{\Sigma}_{sa} + T\dot{\Sigma}_{iso}$$

with  $T\dot{\Sigma}_{iso} = \dot{W}_{hv} - T\dot{\Sigma}_{sa} \geq 0$ . The above equation allows for the following thermodynamic interpretation. At the steady state, to maintain the free energy storage, that is keeping the self-assembly reactions away from equilibrium ( $T\dot{\Sigma}_{sa} > 0$ ), part of the power absorbed by the photoisomerization steps ( $\dot{W}_{hv}$ ) needs to be transferred to the self-assembly ones, allowing them to dissipate.

This means that the supramolecular pump operates as a (thermal) engine transducing free energy from the photons to the self-assembly processes through the photoisomerization processes. Therefore, free energy storage, and consequently unidirectional motion of the ring-axle pairs, are sustained by light energy absorption.

At the steady state  $v_1 = -v_3 = v_{cy}$ , thus  $T\dot{\Sigma}_{sa} = -v_{cy}(\Delta\mu_1 - \Delta\mu_3)$ . Upon integration of this equation over the time it takes for a mole of rings to complete one cycle ( $\tau_{cy} = 1/v_{cy}V$ ) and multiplying by the volume, we find that the free energy dissipated by the motor per cycle of operation at the steady state reported in the main text is given by:

$$T\Delta_{cy}\Sigma_{sa} = -(\Delta\mu_1 - \Delta\mu_3)$$

In turns, this value also sets a limit to the amount of work which self-assembly steps can perform per mole of rings which complete one pumping cycle.

### 5.3.2 Energy storage

The free energy density stored in the self-assembly steps at steady state can be defined by virtue of the timescale separation between the relaxation times of the self-assembly steps and the isomerization ones. In fact, once the photon flow is stopped, the self-assembly steps reach their (local) equilibrium much faster than the isomerization reactions, which can equilibrate only via the very slow thermal relaxation steps. Therefore, the relative amounts of *E* and *Z* species are preserved. In these conditions, the free energy released by the relaxation to equilibrium of the self-assembly steps alone corresponds to the fraction of free energy they stored. In the following the suffix “dark” indicates that the quantity is referred to the local equilibrium, while the other quantities are considered at the dissipative steady state. The following mass balances hold true upon relaxation to the local equilibrium:

$$\begin{aligned} [EC] + [E] &= [EC]_{dark} + [E]_{dark} \\ [ZC] + [Z] &= [ZC]_{dark} + [Z]_{dark} \\ [EC] + [ZC] + [C] &= [EC]_{dark} + [ZC]_{dark} + [C]_{dark} \end{aligned}$$

Moreover, for the concentration at local equilibrium (in dark) the following relations hold true:

$$K_E = \frac{k_1}{k_{-1}} = \frac{[EC]_{dark}}{[E]_{dark}[C]_{dark}}$$

$$K_Z = \frac{k_3}{k_{-3}} = \frac{[ZC]_{dark}}{[Z]_{dark}[C]_{dark}}$$

With the above five equations, we can uniquely compute the (local) equilibrium concentrations ( $[i]_{dark}$ ) by just knowing the steady state concentration in an experimental regime and the in/out kinetic rate constants of the self-assembly steps. The free energy stored in the self-assembly steps per unit volume at the steady state reached in any experimental regime as reported in the main text can then be computed as:

$$\Delta G_{sa} = G - G_{dark}$$

Since the Gibbs free energy of the system per unit of volume is  $G = \sum_i [i](\mu_i - RT)$ , then the stored energy density becomes:<sup>9</sup>

$$\Delta G_{sa} = \sum_i [i](\mu_i - RT) - [i]_{dark}(\mu_{i,dark} - RT) = RT \sum_i [i] \ln \frac{[i]}{[i]_{dark}} - [i] + [i]_{dark}$$

which was used to calculate the energy storage reported in the main text.

#### 5.4 Energy Transduction Efficiency

The efficiency at which the motor, at steady state, converts the light energy into chemical energy available to the self-assembly reactions can be defined in two ways. The first, reported in the main text ( $\eta$ ), consists in evaluating the fraction of work performed by the radiation (free energy) on the system which is successfully transferred to the self-assembly steps:

$$\eta = \frac{T\dot{\Sigma}_{sa}}{\dot{W}_{hv}}$$

This quantity is bounded between 0 and 1 and, being based on the free energy gradient generated by the radiation ( $\langle \mu_{hv} \rangle$ ), can be directly compared between different motors regardless of the provided fuel. For example, the same quantity computed for a chemically driven rotary motor results to be 5 orders of magnitude lower.<sup>10</sup> This can be explained by considering that the chemically driven rotary motor synthesized by the Leigh group works by transducing free energy only in form of information, while here  $T\Delta_{cy}\Sigma_{sa}$  also have an energetic component due to the energy ratchet mechanism.

Additionally, in the spirit of Carnot's efficiency of thermal machines, we can evaluate the ratio between the free energy transduced to the self-assembly steps per unit time and unit volume (dissipation  $T\dot{\Sigma}_{sa}$ ), and the heat absorbed from the radiation (the hot reservoir) per unit time and unit volume ( $\dot{Q}_{hv}$ ), according to the following equation:

$$\eta_2 = \frac{T\dot{\Sigma}_{sa}}{\dot{Q}_{hv}} \leq \langle \eta_C \rangle$$

Where  $\dot{Q}_{hv} = \frac{N_A h c}{\lambda V} q_{n,p} (1 - 10^{-b \sum_i \varepsilon_i [i]})$  is the total power absorbed by the sample in the unit time and volume. The fact that this efficiency is upper limited by the average Carnot efficiency (proof in section 5.4.1) makes  $\eta_2$  an interesting quantity to understand how close the motor, seen as a thermal engine, works to the theoretical limit imposed by Carnot efficiency. The comparison is done in Table S8, which shows that at best this motor reaches 0.04% of Carnot efficiency and decreases with the photon flow. All the considerations in the main text aimed at rationalizing the trend of the energy transduction efficiency ( $\eta$ ) hold for the Carnot-like efficiency  $\eta_2$ .

**Table S8.** Ratio between the average Carnot-like and Carnot's efficiency ( $\eta_2/\langle \eta_C \rangle$ ) at the investigated photon flows.

	$q_{n,p}$ (Einstein s <sup>-1</sup> )			
	$4.4 \times 10^{-9}$	$1.1 \times 10^{-8}$	$2.2 \times 10^{-8}$	$4.4 \times 10^{-8}$
$\eta_2/\langle \eta_C \rangle$ (%)	0.04	0.03	0.02	0.01

#### 5.4.1 Proof of the bound $\eta_2 \leq \langle \eta_C \rangle$

Consider the following expression of the Second Law of thermodynamics as it applies for the system under study inside a volume element  $dV_{cyl}(r)$  at the steady state:

$$T\dot{\Sigma}(r) = T\dot{\Sigma}_{iso}(r) + T\dot{\Sigma}_{sa} = \frac{d\dot{W}(r)}{dV_{cyl}(r)} - T\dot{\Sigma}_{sa} + T\dot{\Sigma}_{sa} = \dot{Q}_{hv}(r)\eta_C(r) - T\dot{\Sigma}_{sa} + T\dot{\Sigma}_{sa} \geq 0$$

where  $T\dot{\Sigma}_{iso}(r)$  and  $T\dot{\Sigma}_{sa}$  are both positive quantities and  $\dot{Q}_{hv}(r) = N_A h \nu \frac{dq_{n,p}(r)}{dV_{cyl}(r)}$  is the heat per unit volume which is absorbed by the system in the volume element. Note that  $T\dot{\Sigma}_{sa}$  does not depend on  $r$  due to the homogeneity in concentrations. From the above equation follows that:

$$0 \leq \frac{T\dot{\Sigma}_{sa}}{\dot{Q}_{hv}(r)\eta_C(r)} = 1 - \frac{T\dot{\Sigma}_{iso}(r)}{\dot{Q}_{hv}(r)\eta_C(r)} \leq 1$$

and therefore  $\eta_2(r) \leq \eta_c(r)$ , with  $\eta_2(r) = \frac{T\dot{\Sigma}_{sa}}{\dot{Q}_{hv}(r)}$ .

By averaging over the entire system (see section 5.2) we have:

$$\langle \eta_2 \rangle = T\dot{\Sigma}_{sa} \left\langle \frac{1}{\dot{Q}_{hv}} \right\rangle \leq \langle \eta_c \rangle$$

And by virtue of the inequality holding between the harmonic and the arithmetic mean of a positive defined function, we have that:

$$\left\langle \frac{1}{\dot{Q}_{hv}} \right\rangle \geq \frac{1}{\langle \dot{Q}_{hv} \rangle} \equiv \frac{1}{\dot{Q}_{hv}}$$

and therefore  $T\dot{\Sigma}_{sa} \left\langle \frac{1}{\dot{Q}_{hv}} \right\rangle \geq \frac{T\dot{\Sigma}_{sa}}{\langle \dot{Q}_{hv} \rangle} = \frac{T\dot{\Sigma}_{sa}}{\dot{Q}_{hv}} = \eta_2$ , which proves the inequality  $\eta_2 \leq \langle \eta_c \rangle$ .

## 7. References

- Corra, S., Casimiro, L., Baroncini, M., Groppi, J., La Rosa, M., Tranfić Bakić, M., Silvi, S. & Credi, A. Artificial Supramolecular Pumps Powered by Light. *Chem. Eur. J.* **27**, 11076–11083 (2021).
- L. Vetráková, V. Ladányi, J. A. Anshori, P. Dvořák, J. Wirz, D. Heger The Absorption Spectrum of cis-Azobenzene. *Photochem. Photobiol. Sci.* **16**, 1749–1756 (2017).
- V. Ladányi, P. Dvořák, J. A. Anshori, L. Vetráková, J. Wirz, D. Heger Azobenzene Photoisomerization Quantum Yields in Methanol Redetermined. *Photochem. Photobiol. Sci.* **16**, 1757–1761 (2017).
- Astumian, R. D. & Bier, M. Mechanochemical Coupling of the Motion of Molecular Motors to ATP Hydrolysis. *Biophys. J.* **70**, 637-653 (1996).
- Onsager, L. Reciprocal Relations in Irreversible Processes. I. *Phys. Rev.* **37**, 405–426 (1931).
- Mausser, H. & Gauglitz, G. *Photokinetics: theoretical fundamentals and applications* (Elsevier, 1998).
- Demirel, Y. & Gerbaud, V. Chapter 8: Chemical Reactions. *Nonequilibrium Thermodynamics Transport and Rate Processes in Physical, Chemical and Biological Systems* (Elsevier, 2019).
- a) Ries, H. & McEvoy, A. J. Chemical Potential and Temperature of Light. *J. Photochem. Photobiol. A* **59**, 11–18 (1991); b) Gräber, P. & Milazzo, G. *Bioenergetics* (Birkhäuser, 1997); c) P. Würfel, P. & Würfel, U. *Physics of Solar Cells: From Basic Principles to Advanced Concepts* (Wiley-VCH, 2016); d) Penocchio, E., Rao, R. & Esposito, M. Nonequilibrium Thermodynamics of Light-Induced Reactions. *J. Chem. Phys.* **155**, 114101 (2021).
- The relation is obtained by considering that  $\sum_i [i]_{dark} \mu_{i,dark} = \sum_i [i] \mu_{i,dark}$ , which can be proven via chemical reaction network techniques by noticing that the vector with elements  $\mu_{i,dark}$  is a left-null vector of the stoichiometric matrix when only self-assembly steps are considered.
- a) Wilson, M. R., Sola, J., Carlone, A., Goldup, S. M., Lebrasseur, N. & Leigh, D. A. An Autonomous Chemically Fueled Small-Molecule Motor. *Nature* **534**, 235-240 (2016); b) Amano, S., Esposito, M. Kreidt, E., Leigh, D. A., Penocchio, E. & Roberts, B. M. W. Insights from an Information Thermodynamics Analysis of a Synthetic Molecular Motor. *Nat. Chem.* (2022) doi: 10.1038/s41557-022-00899-z.